Research Article | Vol. 9, No. 12 | 1 Dec 2018 | BIOMEDICAL OPTICS EXPRESS 6545

Biomedical Optics EXPRESS

In vivo label-free confocal imaging of the deep mouse brain with long-wavelength illumination

Fei Xia,[1,2,5,*] Chunyan Wu,[1,3,5] David Sinefeld,[1] Bo Li,[1] Yifan Qin,[1,4] and Chris Xu[1]

[1]*School of Applied and Engineering Physics, Cornell University, Ithaca, NY 14853, USA*
[2]*Meinig School of Biomedical Engineering, Cornell University, Ithaca, NY 14853, USA*
[3]*College of Veterinary Medicine, Cornell University, Ithaca, NY 14853, USA*
[4]*National Key Laboratory of Science and Technology on Tunable Laser, Harbin Institute of Technology, Harbin 150080, China*
[5]*These authors contributed equally.*
**fx43@cornell.edu*

Abstract: Optical microscopy is a valuable tool for *in vivo* monitoring of biological structures and functions because of its non-invasiveness. However, imaging deep into biological tissues is challenging due to the scattering and absorption of light. Previous research has shown that 1300 nm and 1700 nm are the two best wavelength windows for deep brain imaging. Here, we combined long-wavelength illumination of ~1700 nm with reflectance confocal microscopy and achieved an imaging depth of ~1.3 mm with ~1-micrometer spatial resolution in adult mouse brains, which is 3-4 times deeper than that of conventional confocal microscopy using visible wavelength. We showed that the method can be added to any laser-scanning microscopy with simple and low-cost sources and detectors, such as continuous-wave diode lasers and InGaAs photodiodes. The long-wavelength, reflectance confocal imaging we demonstrated is label-free, and requires low illumination power. Furthermore, the imaging system is simple and low-cost, potentially creating new opportunities for biomedical research and clinical applications.

© 2018 Optical Society of America under the terms of the OSA Open Access Publishing Agreement

1. Introduction

Noninvasive imaging deep into scattering biological tissues with high spatial resolution is important for biomedical research and clinical applications. Optical microscopy is an important tool for visualization of cellular structure and function [1,2], medical diagnosis [3], optical metrology [4], etc. However, the image quality is degraded when the imaging depth becomes largely due to the scattering and absorption of the tissue. Mouse brain is a classic example of the scattering biological tissue, and high resolution, deep, non-invasive imaging of the mouse brain is still challenging today despite the progress in the last 2 to 3 decades [5].

To image deep into a scattering biological tissue with high spatial resolution (i.e., close to diffraction-limited optical resolution), one typically needs to separate the contribution of the ballistic photons within the focal volume from that of out-of-focus photons everywhere else. A variety of techniques have been developed to accomplish this task, including the use of confocal pinhole [6], nonlinear excitation [7,8], and coherence gating [9,10]. Previous research has shown that multiphoton microscopy (MPM) is advantageous in *in vivo* deep brain imaging because of its spatially-confined excitation volume and long excitation wavelength. Imaging mouse brains with 2-photon microscopy (2PM) [11], and 3-photon microscopy (3PM) [8,12] at beyond 1-mm depth *in vivo* were reported by leveraging the optimal wavelength windows for deep tissue penetration at 1.3 μm and 1.7 μm, determined by the combined effects of the scattering and absorption of brain tissues *in vivo* [8,13]. By moving the imaging window to ~1.7 μm, researchers have also shown that optical coherence

#347550 https://doi.org/10.1364/BOE.9.006545
Journal © 2018 Received 11 Oct 2018; revised 6 Nov 2018; accepted 20 Nov 2018; published 29 Nov 2018

Biomedical Optics EXPRESS

tomography (OCT) [14] and optical coherence microscopy (OCM) [15] could achieve an imaging depth up to 1.2 mm in mouse brain. On the other hand, either time or coherence gating is needed for depth discrimination with optical-coherence-based imaging methods, which typically requires a broad-band source and an optical interferometer setup. Compared to MPM, OCT, and OCM, confocal microscopy is relatively easier to implement. Particularly, reflectance confocal microscopy (RCM), a label-free confocal modality has proven its capability in brain imaging *in vivo* by observing myelinated axons [16] down to ~400 μm using illumination at 400-600 nm. RCM has also been widely accepted in the clinical settings because it is simple, low-cost, and label-free. Thus, development of deep RCM has promise for clinical applications such as monitoring blood flow in patients [17], measuring blood cells [18], and detecting early cancers [19,20].

In this paper, we demonstrate *in vivo* long wavelength reflectance confocal microscopy (LW-RCM) for mouse brain imaging at more than 1.2-mm depth with illumination wavelength at ~1.7 μm, imaging through the entire neocortex and the external capsule, and reaching the subcortical region of the mouse brain. Furthermore, we compared the image contrast by performing simultaneous reflectance confocal and third-harmonic generation (THG) imaging. The long wavelength confocal microscopy demonstrated in this paper is simple and robust; and achieves high spatial resolution (~1 μm) at depth comparable to MPM and OCT, which is 3 to 4 times deeper than previously reported imaging depth of reflectance confocal imaging [16]. The method is label-free and can be easily added to any long wavelength 2PM and 3PM by the addition of a confocal detector. More broadly, the demonstrated method is promising for biomedical research and clinical applications where label-free, high spatial resolution imaging deep within tissue is required.

2. Setup and methods

2.1 Imaging setup

The images were taken with a home-built laser scanning microscope with a high-numerical aperture objective (Olympus XLPLN25XWMP2, 25X, NA 1.05), see Fig. 1(a). The back aperture of the objective is overfilled to make full use of the numerical aperture (NA). The signal is epi-collected through the objective. A combination of a polarization beam splitter (PBS) and a λ/4-waveplate was installed to separate the illumination and back-scattered light, which also suppresses the spurious reflection from the various optical components along the beam path. For simultaneous imaging with LW-RCM and THG, we used a non-collinear optical parametric amplifier pumped by a chirped-pulse amplification system (Monaco, Opera-F, Coherent), operating at 1650 nm. A fiber-coupled InGaAs PMT (PMT 1, H10330C-75, Hamamatsu) and an ultra bialkali PMT (PMT 2, R7600-200, Hamamatsu) were used for the detection of the reflectance confocal signal and the THG signal, respectively. For demonstration of the simplicity of LW-RCM, we also used continuous-wave (CW) diode lasers as the illumination source, operating at 1610 nm with a distributed feedback laser (DFB) laser (79800D, ILX Lightwave), 1630 nm (Fabry-Perot Laser Diode, FPL1059P, Thorlabs), and 1310 nm (Fabry-Perot Laser Diode, FPL1053P, Thorlabs), and an InGaAs photodiode (PDA10CS, Thorlabs) as the detector. The back-scattered light is de-scanned and refocused by a 75-mm achromatic lens into the multimode fiber (MMF, 25 μm-diameter core, Thorlabs), which also serves as the confocal aperture. The polarizer before the multimode fiber was used to further suppress the signal from the spurious reflection from the optical components when the extinction ratio of the PBS is not enough. Image acquisition and stage control were performed using ScanImage running on MATLAB (MathWorks). The PMT current is converted to voltage using a trans-impedance amplifier (C7319, Hamamatsu) with the gain set to 10^5 V/A. The amplifier gain for the PD is ~1.5×10^6 V/A based on the signal strength and the bandwidth consideration. Analog-to-digital conversion was performed by a data acquisition card (NI PCI-6115, National Instruments).

Biomedical Optics EXPRESS

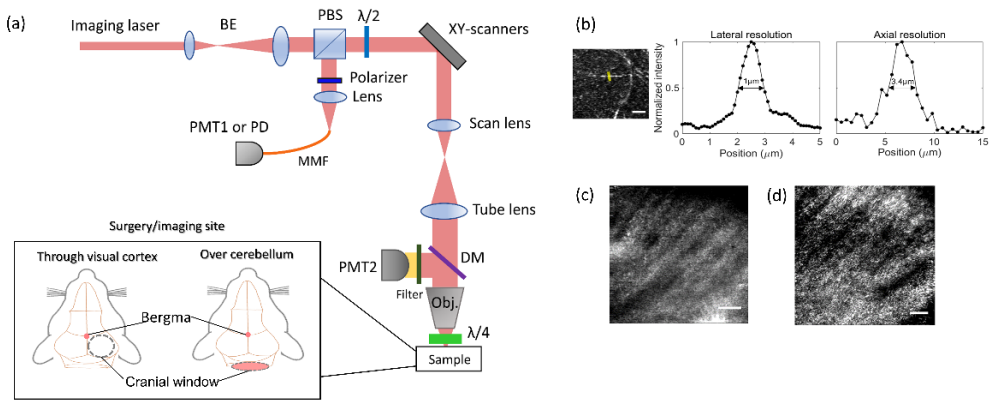

Fig. 1. (a) Schematic illustration of the imaging system. BE: beam expander, PBS: polarizing beam splitter, λ/2: half-waveplate, λ/4: quarter-waveplate, MMF: multimode fiber, DM: dichroic mirror. The focal length for the scan lens and tube lens is 150 mm and 750 mm, respectively. The photocathodes for PMT1 and PMT2 are, respectively, InGaAs and ultra bialkali. An InGaAs photodiode (PD) is also used for some of the experiments. Schematic illustrations of the imaging sites. Left side: surgery/imaging site for Figs. 1-3 and 5; right side: surgery/imaging site of the cerebellum of the mouse brain for Fig. 4. (b) Lateral and axial intensity profiles of axons at 400 μm depth (along the yellow line in the image on the left). The FWHMs are indicated in the plots. Scale bar: 10 μm. (c) mouse brain image obtained when mounted with common coverslip glass window. Scale bar: 30 μm. (d) mouse brain image obtained when mounted with quarter-waveplate window. Scale bar: 30 μm.

2.2 Animal preparation

All animal procedures were performed with the approval of the Cornell Institutional Animal Care and Use Committee (IACUC) and under the guidance of the Cornell Center for Animal Resources and Education.

For all adult mice (C57BL/6J, Male, Age: 12-32 weeks), imaging sessions were conducted at least one week after the surgery for tissue inflammation to disappear. The craniotomy with conventional glass window was described in [12]. For the mouse surgery preparation for imaging through visual cortex, we opened windows of 5 mm in diameter, centered at 2 mm lateral, and 2.5 mm caudal from the bregma point over the visual cortex. For the mouse preparation in cerebellum, we opened windows of 3 mm in diameter, centered at 0 mm lateral and 7 mm caudal from the bregma point. One of the vexing problems for RCM is the spurious reflection from the optical components in the beam path. While a PBS and λ/4-waveplate combination can largely suppress the spurious reflection from the optics before the λ/4-waveplate, we found that the back-reflection from the objective lens severely limits our ability to image deep. We used a 5 × 5 mm square-shaped λ/4-waveplate (WPQ501, Thorlabs) instead of the normal cover-glass as the cranial window. The λ/4-plate cranial window has thickness close to a conventional cover glass (~170 μm), making it compatible with most microscope objectives. Since the λ/4-plate is placed after the objective lens (Fig. 1(a)), our PBS and λ/4-plate combination largely eliminates the back-reflection from the objective lens when illuminated at 1650 nm, see Fig. 1(c,d). Figure 1(c) shows an image at white matter area with conventional cranial window and a quarter waveplate before the objective. Figure 1(d) is an image at white matter area with quarter-waveplate mouse cranial window. The back-reflection from the objective and other optical components are removed completely by positioning the quarter-waveplate underneath the objective lens so that no background subtraction is needed.

Biomedical Optics EXPRESS

2.3 In vivo imaging

The mouse is placed on a motorized stage (M-285, Sutter Instrument Company) for axial scanning. Because the index of refraction of brain tissue [21,22] is larger than that of the immersion medium (water or heavy water), the actual imaging depth within the tissue is ~5–10% larger than the depth measurement indicated (i.e., the raw axial movement of the objective) here. Deuterium oxide (i.e., heavy water, D_2O) is used as the objective immersion medium to reduce the absorption caused by water (H_2O) [8] when imaging at 1550 nm, 1610 nm, and 1650 nm. For the experiment confirming the long wavelength advantage (see Fig. 4(c)), we used an achromatic quarter waveplate (AQWP10M-1600, Thorlabs, retardance performance confirmed by the simulation data from Thorlabs at 1060 nm and 1630 nm and by experimental verification at 1060 nm) between the dichroic mirror and the tube lens, and a conventional cover glass is used for the cranial window [12].

3. Results and discussions

3.1. Comparison between LW-RCM and THG in vivo imaging

THG microscopy [23] has the capability for label-free imaging [24]. Imaging blood vessels [25] and myelinated axons [26] have been demonstrated previously with THG. For LW-RCM, the main source of contrast is the linear refractive index mismatch [27]. For THG microscopy, the main image contrast is generated from the third-order nonlinear susceptibility $\chi^{(3)}$ mismatch or linear refractive index difference [26,28]. When the refractive indices of the sample and the surrounding environment are identical at the third-harmonic frequency,

$$P_{3\omega} \propto P_o^3 \left|\chi_s^{(3)} - \chi_e^{(3)}\right|^2 \tag{1}$$

where $P_{3\omega}$ is the THG signal. P_0 is the intensity of the fundamental wave. $\chi_s^{(3)}$ and $\chi_e^{(3)}$ are, respectively, the third-order nonlinear susceptibility of the sample and the surrounding environment. Equation (1) indicates that the THG signal results from the difference of the third-order nonlinear susceptibility of the sample and their environment if the linear refractive indices at the third-harmonic frequency are the same. This is different from the mechanism of the signal generation in LW-RCM, where the main source of contrast comes from the variations of linear refractive index at the fundamental frequency [27]. Therefore, it is not surprising that noticeable differences were observed in our comparisons between THG microscopy and LW-RCM.

To compare the images obtained by LW-RCM and THG imaging, we first conducted simultaneous imaging using LW-RCM and THG microscopy. We used the same optical path for the illumination while the signals were detected through two different optical paths separated by a dichroic mirror (Fig. 1(a)). Images of the mouse brain at approximately 100 μm step from ~100 μm down to more than 800 μm were shown in Fig. 2(a).

Biomedical Optics EXPRESS

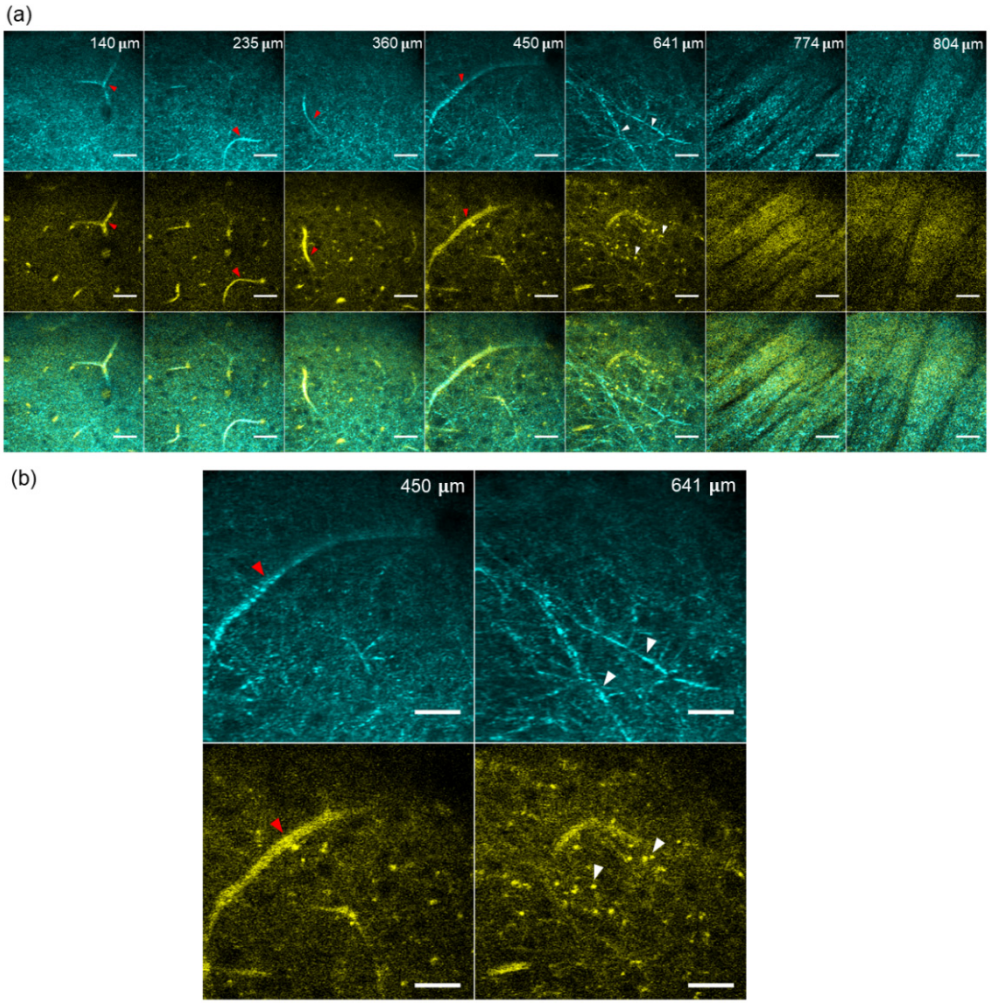

Fig. 2. Comparison of reflectance confocal and THG images through the mouse visual cortex. (a) Reflectance confocal (top, cyan), THG (middle, yellow) and merged reflectance confocal and THG images (bottom) at various depths: 140 µm, 235 µm, 360 µm, 450 µm, 641 µm, 774 µm and 804 µm. Myelinated axons are indicated with white arrows; blood vessels are indicated with red arrows. Scale bars are 30 µm. (b) Enlarged images at depth 450 µm and 641 µm from (a) are shown, where blood vessels are indicated in red and myelinated axons are indicated in white. Scale bars are 30 µm.

All the images share some similarities in the blood vessels that are orientated perpendicular to the optical axis. For the vessels that are oriented parallel to the optical axis, they appear as bright, circular-shaped features in the THG microscopy, shown in images at 140 µm and 235 µm; while they appear as dark void in the LW-RCM images. Within the external capsule, from ~774 µm to 804 µm, the images are well-correlated: the stripe patterns of the white matter are the same. This indicates that LW-RCM of the white matter may provide comparable spatial information as THG microscopy for myelinated axons. Though LW-RCM revealed less capillaries (Fig. 2), it appears to be more sensitive to detect sparsely distributed myelinated axons, e.g., at 640 µm depth, a region above the white matter. In Fig. 3, we also observed similar differences in imaging the myelinated axons in the cerebellum. Cerebellum is an important brain region to study. It contains more neurons than the total from the rest of the brain but takes up only 10% of the total brain volume [29]. The cerebellum plays an important role for motor planning and execution, and may even be involved in higher

cognitive functions. However, cerebellum is a brain region with dense myelinated fibers, and is challenging for optical imaging because of the strong scattering. Imaging cerebellum structure, especially axon fibers, may help us understand cerebellum organizations and connections with other brain regions. We performed simultaneous *in vivo* THG and LW-RCM imaging at different depths (mouse: LriglcreER/Rosa 26Ai14, 32-36 weeks). Note that the LW-RCM image at 800 μm depth is quite different from the THG image. The LW-RCM image shows more up-down oriented fibers, while the THG image shows more left-right oriented fibers.

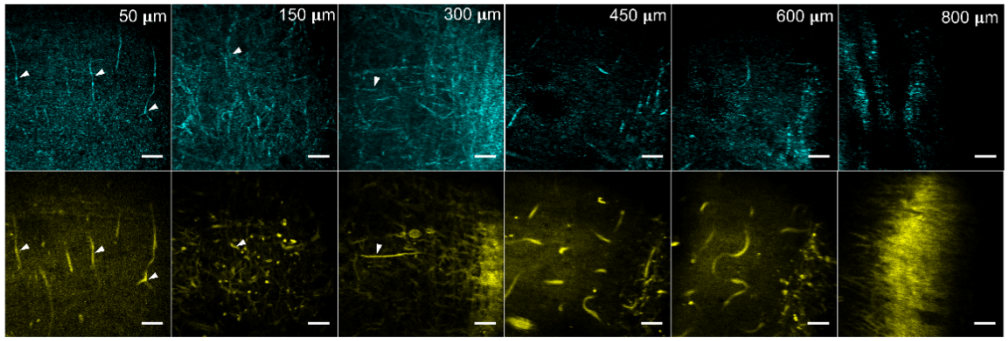

Fig. 3. Comparison of LM-RCM (top, cyan) and THG images (middle, yellow) at different depths in mouse cerebellum: 50 μm, 150 μm, 300 μm, 450 μm, 600 μm and 800 μm. Myelinated axons are indicated with white arrows. Scale bar: 30 μm.

Since water absorption dominates at wavelength greater than ~1200 nm in the mouse brain *in vivo*. For example, the absorption coefficients of oxygenated blood and deoxygenated blood are approximately the same in the long wavelength regions [30,31]. The absorption difference between the oxygenated blood and deoxygenated blood does not contribute significantly to the image contrast. Instead, refractive index mismatch gives rise to stronger contrast [27], for example, fat and water refractive index difference mainly results in features with high lipids concentration such as myelinated axons. For THG imaging, the image contrast mainly comes from the difference in the third-order nonlinear susceptibility ($\chi^{(3)}$) between the two sides of the focal plane of the excitation beam. For *in vivo* brain imaging, blood vessels and myelinated axons are the main features that produces significant THG signal [32]. While the images obtained by LW-RCM and THG microscopy have a lot of similarities, they are not identical due to the different contrast mechanisms discussed before. Therefore, simultaneous THG and LW-RCM might reveal extra information regarding the tissue properties. The white-matter tracts (i.e., the densely packed, myelinated axons) are the structural connective scaffolding of the brain [33]. They were shown to play an important role in modulating neural circuits and brain function [33], such as in the Multiple Sclerosis disease [34]. Our results show that we can image myelinated axons with high spatial resolution *in vivo* in the white matter region of the mouse brain with simple LW-RCM.

Even for deep white matter imaging, relatively low optical power is required, at approximately tens of microwatts under the objective lens when using a PMT as the detector (frame rate 0.23 Hz). This power level is orders of magnitude lower than what is required for THG microscopy, which typically requires energetic femtosecond pulses with average power of tens of milliwatts in order to acquire images at the same depth.

3.2 Deep mouse brain imaging with LW-RCM

To explore the maximum imaging depth *in vivo*, we also acquired 3D imaging stack within the mouse brain. Image sections at various depths are shown in Fig. 4(a), (See also Visualization 1). We were able to image at the maximum imaging depth of ~1.3 mm, through

Biomedical Optics EXPRESS

the entire neocortex and the external capsule, reaching the subcortical region of the mouse brain.

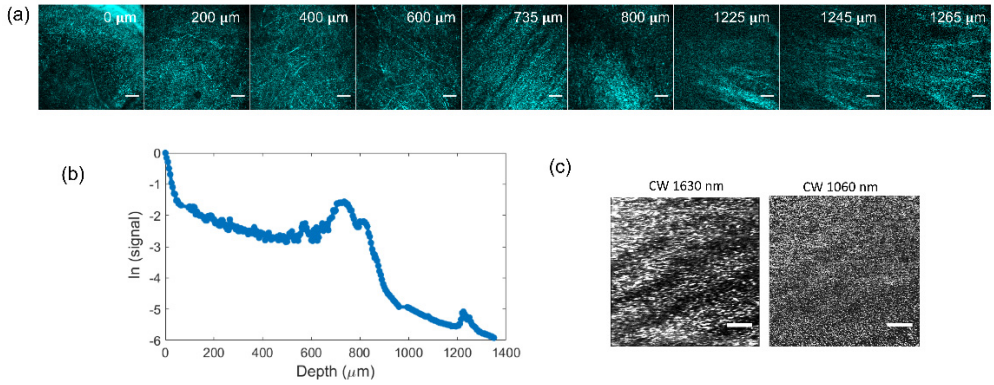

Fig. 4. (a) *In vivo* reflectance confocal images at various depths through the mouse visual cortex. Scale bar 30 µm. (b) Semi-logarithmic plot of reflectance confocal signal (normalized to the signal at the surface and to the optical power) as a function of imaging depth. (c) Images at 770 µm obtained by CW lasers at 1630 nm (left) and 1060 nm (right). Scale bar 30 µm.

The semi-logarithmic plot of the reflectance signal of the mouse brain as a function of the imaging depth is shown in Fig. 4(b). The bump in signal level at 700 to 850 µm indicates the region for the external capsule (EC) of the brain. Since the greatest source of contrast in reflectance confocal images is the difference of refractive index [27], the large difference of refractive index between the white matter and cortex/surrounding tissue causes the increased signal level at the white matter region. We can estimate the white matter thickness to be ~150 µm. We also observed another fiber tracts layer from 1.2 mm to 1.3 mm below the brain surface (alveus of hippocampus). At the depth of 1-1.2 mm, few myelinated axons were observed (Visualization 1); however, we can still observe myelinated axons within 100 µm below the white matter (See Visualization 1). With the λ/4-waveplate cranial window, we can largely eliminate the back-reflection from the objective at 1650 nm, which helped us greatly in pushing the penetration depth (See Fig. 1(c, d)).

To confirm the advantage of the LW-RCM for deep imaging, wavelengths at 1060 nm (QFBGLD-1060-40, QPHOTONICS, LLC.) and 1630 nm were used to image the same white matter *in vivo* (Fig. 4(c)). Note that for this experiment, an achromatic quarter waveplate was installed before the objective and a conventional glass cranial window was used. As there will be residual spurious reflection from the optics, we performed background subtraction with and without mouse. Although we used 20 times more average power at 1060 nm (~2 mW) than that at 1630 nm (100 µW), it is not possible to observe the structural details of the white matter at 770 µm depth with 1060 nm illumination. This direct comparison unequivocally demonstrated the advantage of the LW-RCM for deep brain penetration.

Biomedical Optics EXPRESS

3.3 Demonstration of simplicity

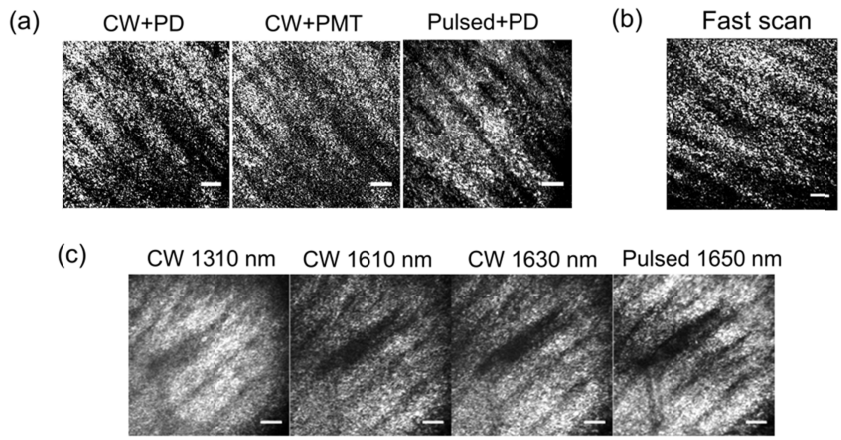

Fig. 5. (a) White matter image at ~700 μm depth acquired with different combination of detectors and laser sources through the mouse visual cortex. CW + PD: CW laser illumination at 1630 nm with InGaAs PD as detector; CW + PMT: CW laser illumination at 1630 nm with InGaAs PMT as detector; Pulsed + PD: pulsed laser illumination at 1650 nm with InGaAs PD as detector. (b) *In vivo* mouse white matter image at depth of 700 μm obtained using 8 kHz resonant scanner (RESSCAN-GEN, Cambridge Inc.) at frame rate of 30 Hz, scale bar: 30 μm. (c) Confocal images of white matter under CW and pulsed laser illumination with the same power at 1310 nm, 1610 nm, 1630 nm, and 1650 nm at ~800 μm. The scale bars are 30 μm.

Imaging the white matter *in vivo* has broad applications in disease diagnosis [35–37] and neuroscience studies [38–40]. White matter structure is expected to be modified due to training or experience because the degree of myelination is modulated by the neuronal activity along the axon [38]. The simplicity and low-cost nature of the LW-RCM system may open new opportunities for label-free, long-term, *in vivo* monitoring of the white matter structures. Here, we demonstrate the possibility of using compact and robust detectors and sources such as InGaAs photodiodes (PDs) and CW diode lasers for LW-RCM. We first compared the images of white matter region collected by the PMT and the PD with the pulsed laser in Fig. 5(a). The brightness of the images obtained with ~30 μW (power at the surface of the mouse brain) using the PMT is comparable to images obtained with ~15 mW using the PD (Fig. 5(a)). The results show that the quality of images is comparable, with much higher power requirements for the PD detector due to the lower gain for the detected signal. Using an avalanche PD might help reducing the power requirement. The optical power and integration time are tuned based on the detector gain and detector type. In Fig. 5(c), we show the confocal images of white matter under CW and pulsed laser illumination with the same power at 1310 nm, 1610 nm, 1630 nm and 1650 nm. We demonstrated a variety of laser sources as illumination source in our paper in Fig. 5(c): for the femtosecond pulsed laser at 1650 nm, the coherence length is ~10 μm; for the multimode Fabry-Perot Laser Diodes at 1630 nm, the coherence length is ~80 μm; and for a single mode DFB laser at 1610 nm, the coherence length is ~3 m. Though the coherence length is varied by many orders of magnitude, it does not appear to influence the white matter image. The *in vivo* mouse brain images obtained at the long wavelengths from ~1300 nm to ~1700 nm all produced good image contrast, making LW-RCM a practical tool for imaging the white matter tracts within a living mouse. There are potential benefits of working with several wavelengths simultaneously. For example, the thickness of myelin layers or other fine structures can be measured by recording the reflected light signal across a range of illumination wavelengths [4]. Low cost CW diode lasers are clearly adequate as the illumination source for deep

Biomedical Optics EXPRESS

confocal imaging at the long wavelength windows. As the power requirement of mouse brain white matter imaging is low in LW-RCM, we also demonstrate the fast imaging capability in Fig. 5(b) with resonant scanners (RESSCAN-GEN, Sutter Instrument). we achieved a frame rate of 30 Hz with 512 × 512 pixels per frame and imaged the white matter of the mouse brain *in vivo* using the PMT and CW laser with ~24 mW under the objective. While the power level is much higher than that needed at the lower frame rate (e.g., Fig. 2), it is still comparable to or lower than that used in most multiphoton microscopy.

4. Conclusions

In conclusion, we demonstrated that long-wavelength reflectance confocal microscopy (LW-RCM) is a simple, robust, and low-cost technique for label-free, high-resolution *in vivo* imaging of the mouse brain down to ~1.3 mm depth. We compared the LW-RCM with THG imaging and found that the two imaging methods have some similarities, but not identical. Simultaneous THG and RCM might reveal extra information regarding the tissue properties. We confirmed the advantage of LW-RCM by comparing images acquired at different wavelengths. We showed the simplicity of this method by using a photodiode as the detector or CW diode lasers as the illumination source. Furthermore, LW-RCM requires CW illumination at low power when imaging with a PMT. Comparing to other label-free methods such as THG, OCM, coherent anti-Stokes Raman scattering (CARS) microscopy, our method does not require expensive laser sources and/or complicated optical setup. Although the focus of this paper is the mouse brain, the long wavelength window investigated is likely to be beneficial for deep imaging of other tissue types. For example, it was demonstrated that long wavelength excitation significantly improves the penetration depth of THG imaging of skin and human tissue [41,42]. The LW-RCM demonstrated in this paper can potentially be translated to other tissue types beyond the brain, for example, skin imaging [40,43,44], cancer diagnosis [45], and dynamic functional imaging, such as blood flow imaging [17]. LW-RCM has the promise to create new opportunities where high-resolution, label-free, deep imaging of tissue structure and function is required.

Funding

National Institutes of Health (NIH) (R21EY026391, U01NS090530).

Acknowledgments

The authors thank Dr. Tianyu Wang and Aaron Mok for their technical help and discussions.

Disclosures

The authors declare that there are no conflicts of interest related to this article.

References

1. G. Cox, *Optical Imaging Techniques in Cell Biology* (CRC Press, 2012).
2. M. Terasaki and M. E. Dailey, "Confocal microscopy of living cells," in *Handbook of Biological Confocal Microscopy* (Springer, 1995), pp. 327–346.
3. J. G. Fujimoto, M. E. Brezinski, G. J. Tearney, S. A. Boppart, B. Bouma, M. R. Hee, J. F. Southern, and E. A. Swanson, "Optical biopsy and imaging using optical coherence tomography," Nat. Med. **1**(9), 970–972 (1995).
4. J. Kwon, M. Kim, H. Park, B. M. Kang, Y. Jo, J. H. Kim, O. James, S. H. Yun, S. G. Kim, M. Suh, and M. Choi, "Label-free nanoscale optical metrology on myelinated axons in vivo," Nat. Commun. **8**(1), 1832 (2017).
5. J. W. Lichtman and W. Denk, "The big and the small: challenges of imaging the brain's circuits," Science **334**(6056), 618–623 (2011).
6. P. Davidovits and M. D. Egger, "Scanning laser microscope," Nature **223**(5208), 831 (1969).
7. W. Denk, J. H. Strickler, and W. W. Webb, "Two-photon laser scanning fluorescence microscopy," Science **248**(4951), 73–76 (1990).
8. N. G. Horton, K. Wang, D. Kobat, C. G. Clark, F. W. Wise, C. B. Schaffer, and C. Xu, "*In vivo* three-photon microscopy of subcortical structures within an intact mouse brain," Nat. Photonics **7**(3), 205–209 (2013).
9. D. Huang, E. A. Swanson, C. P. Lin, J. S. Schuman, W. G. Stinson, W. Chang, M. R. Hee, T. Flotte, K. Gregory, C. A. Puliafito, and et, "Optical coherence tomography," Science **254**(5035), 1178–1181 (1991).

Biomedical Optics EXPRESS

10. J. A. Izatt, M. R. Hee, G. M. Owen, E. A. Swanson, and J. G. Fujimoto, "Optical coherence microscopy in scattering media," Opt. Lett. **19**(8), 590–592 (1994).
11. D. Kobat, M. E. Durst, N. Nishimura, A. W. Wong, C. B. Schaffer, and C. Xu, "Deep tissue multiphoton microscopy using longer wavelength excitation," Opt. Express **17**(16), 13354–13364 (2009).
12. D. G. Ouzounov, T. Wang, M. Wang, D. D. Feng, N. G. Horton, J. C. Cruz-Hernández, Y. T. Cheng, J. Reimer, A. S. Tolias, N. Nishimura, and C. Xu, "In vivo three-photon imaging of activity of GCaMP6-labeled neurons deep in intact mouse brain," Nat. Methods **14**(4), 388–390 (2017).
13. M. Wang, C. Wu, D. Sinefeld, B. Li, F. Xia, and C. Xu, "Comparing the effective attenuation lengths for long wavelength *in vivo* imaging of the mouse brain," Biomed. Opt. Express **9**(8), 3534–3543 (2018).
14. S. P. Chong, C. W. Merkle, D. F. Cooke, T. Zhang, H. Radhakrishnan, L. Krubitzer, and V. J. Srinivasan, "Noninvasive, in vivo imaging of subcortical mouse brain regions with 1.7 $µm$ optical coherence tomography," Opt. Lett. **40**(21), 4911–4914 (2015).
15. M. Yamanaka, T. Teranishi, H. Kawagoe, and N. Nishizawa, "Optical coherence microscopy in 1700 nm spectral band for high-resolution label-free deep-tissue imaging," Sci. Rep. **6**(1), 31715 (2016).
16. A. J. Schain, R. A. Hill, and J. Grutzendler, "Label-free in vivo imaging of myelinated axons in health and disease with spectral confocal reflectance microscopy," Nat. Med. **20**(4), 443–449 (2014).
17. E. Cinotti, L. Gergelé, J. L. Perrot, A. Dominé, B. Labeille, P. Borelli, and F. Cambazard, "Quantification of capillary blood cell flow using reflectance confocal microscopy," Skin Res. Technol. **20**(3), 373–378 (2014).
18. A. Zeidan and D. Yelin, "Reflectance confocal microscopy of red blood cells: simulation and experiment," Biomed. Opt. Express **6**(11), 4335–4343 (2015).
19. A. Scope, U. Mahmood, D. S. Gareau, M. Kenkre, J. A. Lieb, K. S. Nehal, and M. Rajadhyaksha, "In vivo reflectance confocal microscopy of shave biopsy wounds: feasibility of intraoperative mapping of cancer margins," Br. J. Dermatol. **163**(6), 1218–1228 (2010).
20. C. Loo, A. Lin, L. Hirsch, M.-H. Lee, J. Barton, N. Halas, J. West, and R. Drezek, "Nanoshell-enabled photonics-based imaging and therapy of cancer," Technol. Cancer Res. Treat. **3**(1), 33–40 (2004).
21. J. Sun, S. J. Lee, L. Wu, M. Sarntinoranont, and H. Xie, "Refractive index measurement of acute rat brain tissue slices using optical coherence tomography," Opt. Express **20**(2), 1084–1095 (2012).
22. J. Binding, J. Ben Arous, J.-F. Léger, S. Gigan, C. Boccara, and L. Bourdieu, "Brain refractive index measured in vivo with high-NA defocus-corrected full-field OCT and consequences for two-photon microscopy," Opt. Express **19**(6), 4833–4847 (2011).
23. J. Squier, M. Müller, G. Brakenhoff, and K. R. Wilson, "Third harmonic generation microscopy," Opt. Express **3**(9), 315–324 (1998).
24. D. Yelin and Y. Silberberg, "Laser scanning third-harmonic-generation microscopy in biology," Opt. Express **5**(8), 169–175 (1999).
25. M. Rehberg, F. Krombach, U. Pohl, and S. Dietzel, "Label-free 3D visualization of cellular and tissue structures in intact muscle with second and third harmonic generation microscopy," PLoS One **6**(11), e28237 (2011).
26. M. J. Farrar, F. W. Wise, J. R. Fetcho, and C. B. Schaffer, "In vivo imaging of myelin in the vertebrate central nervous system using third harmonic generation microscopy," Biophys. J. **100**(5), 1362–1371 (2011).
27. A. K. Dunn, C. Smithpeter, A. J. Welch, and R. Richards-Kortum, "Sources of contrast in confocal reflectance imaging," Appl. Opt. **35**(19), 3441–3446 (1996).
28. Y. Barad, H. Eisenberg, M. Horowitz, and Y. Silberberg, "Nonlinear scanning laser microscopy by third harmonic generation," Appl. Phys. Lett. **70**(8), 922–924 (1997).
29. R. R. Llina, K. D. Walton, and E. J. Lang, "Cerabellum," in *The Synaptic Organization of the Brain*, G. Shepherd, ed. (Oxford, 2004).
30. A. Roggan, M. Friebel, K. Dö Rschel, A. Hahn, and G. Mu Ller, "Optical properties of circulating human blood in the wavelength range 400-2500 nm," J. Biomed. Opt. **4**(1), 36–46 (1999).
31. M. Friebel, J. Helfmann, U. Netz, and M. Meinke, "Influence of oxygen saturation on the optical scattering properties of human red blood cells in the spectral range 250 to 2,000 nm," J. Biomed. Opt. **14**(3), 034001 (2009).
32. S. Witte, A. Negrean, J. C. Lodder, C. P. J. de Kock, G. Testa Silva, H. D. Mansvelder, and M. Louise Groot, "Label-free live brain imaging and targeted patching with third-harmonic generation microscopy," Proc. Natl. Acad. Sci. U.S.A. **108**(15), 5970–5975 (2011).
33. R. D. Fields, "White matter in learning, cognition and psychiatric disorders," Trends Neurosci. **31**(7), 361–370 (2008).
34. C. Bjartmar, R. P. Kinkel, G. Kidd, R. A. Rudick, and B. D. Trapp, "Axonal loss in normal-appearing white matter in a patient with acute MS," Neurology **57**(7), 1248–1252 (2001).
35. M. D. Budde, J. H. Kim, H.-F. Liang, R. E. Schmidt, J. H. Russell, A. H. Cross, and S.-K. Song, "Toward accurate diagnosis of white matter pathology using diffusion tensor imaging," Magn. Reson. Med. **57**(4), 688–695 (2007).
36. M. Inagaki, E. Yoshikawa, Y. Matsuoka, Y. Sugawara, T. Nakano, T. Akechi, N. Wada, S. Imoto, K. Murakami, and Y. Uchitomi, "Smaller regional volumes of brain gray and white matter demonstrated in breast cancer survivors exposed to adjuvant chemotherapy," Cancer **109**(1), 146–156 (2007).
37. N. D. Prins, E. J. van Dijk, T. den Heijer, S. E. Vermeer, P. J. Koudstaal, M. Oudkerk, A. Hofman, and M. M. B. Breteler, "Cerebral white matter lesions and the risk of dementia," Arch. Neurol. **61**(10), 1531–1534 (2004).
38. J. Scholz, M. C. Klein, T. E. J. Behrens, and H. Johansen-Berg, "Training induces changes in white-matter

Biomedical Optics EXPRESS

architecture," Nat. Neurosci. **12**(11), 1370–1371 (2009).
39. R. C. Gur, B. I. Turetsky, M. Matsui, M. Yan, W. Bilker, P. Hughett, and R. E. Gur, "Sex differences in brain gray and white matter in healthy young adults: correlations with cognitive performance," J. Neurosci. **19**(10), 4065–4072 (1999).
40. M. Huzaira, F. Rius, M. Rajadhyaksha, R. R. Anderson, and S. González, "Topographic variations in normal skin, as viewed by in vivo reflectance confocal microscopy," J. Invest. Dermatol. **116**(6), 846–852 (2001).
41. S.-Y. Chen, H.-Y. Wu, and C.-K. Sun, "In vivo harmonic generation biopsy of human skin," J. Biomed. Opt. **14**(6), 060505 (2009).
42. C.-K. Sun, C.-C. Chen, S.-W. Chu, T.-H. Tsai, Y.-C. Chen, and B.-L. Lin, "Multiharmonic-generation biopsy of skin," Opt. Lett. **28**(24), 2488–2490 (2003).
43. P. Calzavara-Pinton, C. Longo, M. Venturini, R. Sala, and G. Pellacani, "Reflectance confocal microscopy for in vivo skin imaging," Photochem. Photobiol. **84**(6), 1421–1430 (2008).
44. B. Larson, S. Abeytunge, and M. Rajadhyaksha, "Performance of full-pupil line-scanning reflectance confocal microscopy in human skin and oral mucosa in vivo," Biomed. Opt. Express **2**(7), 2055–2067 (2011).
45. R. M. Woodward, B. E. Cole, V. P. Wallace, R. J. Pye, D. D. Arnone, E. H. Linfield, and M. Pepper, "Terahertz pulse imaging in reflection geometry of human skin cancer and skin tissue," Phys. Med. Biol. **47**(21), 3853–3863 (2002).